Magnetic Field Observations on Interhemispheric Conjugate Chains

D. R. Weimer[1,2], C. R. Clauer[1,2], Z. Xu[1,2], S. Coyle[1], and M. D. Hartinger[3]

[1]Center for Space Science and Engineering Research, Virginia Tech, Blacksburg, Virginia, USA
[2]National Institute of Aerospace, Hampton, Virginia, USA
[3]Space Science Institute, Boulder, CO, USA

Key Points:

- Magnetic field measurements are obtained from magnetic conjugate points in both hemispheres
- Under optimal conditions the conjugate magnetic fields are very similar, provided that signs are reversed on two of the vector components
- More often the fields differ due to different seasonal conductivities and asymmetrical driving by the magnetic field in the solar wind

Corresponding author: Daniel Weimer, `dweimer@vt.edu`

Abstract

A chain of magnetometers has been placed in Antartica for comparisons with magnetic field measurements taken in the northern hemisphere. The locations were chosen to be on magnetic field lines that connect to magnetometers on the western coast of Greenland, despite the difficulty of reaching and working at such remote locations. We report on some basic comparisons of the similarities and differences in the conjugate measurements. Our results presented here confirm that the conjugate sites do have very similar (symmetric) magnetic perturbations in a handful of cases, as expected. Sign reversals are required for two components in order to obtain this agreement, which is not commonly known. More frequently, a strong Y component of the Interplanetary Magnetic Field (IMF) breaks the symmetry, as well as the unequal conductivities in the opposite hemispheres, as shown in two examples. In one event the IMF Y component reversed signs twice within two hours, while the magnetometer chains were approaching local noon. This switch provided an opportunity to observe the effects at the conjugate locations and to measure time lags. It was found that the magnetic fields at the most poleward sites started to respond to the sudden IMF reversals 18 min after the IMF reaches the bow shock, a measure of the time it takes for the electromagnetic signal to travel to the magnetopause, and then along magnetic field lines to the polar ionospheres. An additional 9 to 14 min is required for the magnetic perturbations to complete their transition.

Plain Language Summary

Space science research has long relied on magnetometer measurements in the northern hemisphere to detect and observe the flow of currents in the ionosphere and magnetosphere. In the past few years it has become possible to acquire magnetic field measurements in the southern polar region as well, as a result of the placement of a chain of magnetometer stations in a remote part of Antarctica. Each of these magnetometers were placed where the Earth's magnetic field connects to an existing magnetometer in the northern hemisphere, on the western coast of Greenland. The locations follow a roughly north-south meridian in geomagnetic coordinates. These "conjugate" magnetometer chains are useful for observing the similarities and differences between the ionospheric currents flowing in opposite hemispheres as a result of the solar wind's interaction with the Earth's magnetosphere. This paper presents results showing how the inter-hemispheric measurements are very similar in some cases, but only if the signs of two of the vector components are reversed. In other cases the magnetic fields in the northern and southern hemisphere are different, mainly due to the summer-winter differences in conductivity. The conjugate measurement will be useful for future space science research.

1 Introduction

Due to the dipole nature of Earth's magnetic field, electric fields and plasma motions in the outer magnetosphere map to the ionosphere at polar and auroral latitudes in both hemispheres. The resulting currents that flow in the ionosphere can be detected by their magnetic signature on the ground. Ground arrays of magnetometers at high latitudes are particularly useful for monitoring such space weather phenomena, and learning about the interactions between the solar wind, the magnetosphere, and ionosphere. Arrays of instruments in the polar regions can be used to supplement sparse observations from satellites in space. Measurements from polar instruments are also vital to the validation of global numerical models that may be used to describe and forecast space weather phenomena. It is, therefore, increasingly important to deploy arrays of geophysical instruments in polar regions to advance our understanding of the complex electrodynamic interactions that comprise space weather. It is assumed that the magnetometers at conjugate locations (at opposite ends of the magnetic field lines) should similar magnetic perturbations due to the magnetospheric flows, electric fields, and currents. On the other hand, differences should be expected because of the considerable asymmetries between the two hemispheres. For example, solar illumination differences between the summer and winter hemisphere produce large asymmetries in the conductance in the two polar ionospheres (Ostgaard & Laundal, 2012). The magnetic field in the Southern Hemisphere is significantly weaker, which also influences conductivity (Laundal et al., 2017). For these reasons the examination of simultaneous data from both the northern and southern polar regions is very important for understanding the causes and consequences of hemispheric asymmetries and, more broadly, to space science research. The results presented here use data from two ground magnetometer chains that are located at conjugate locations in both hemispheres. The similarities and differences in these data in are examined. This investigation concerns magnetic perturbations varying on timescales on the order of 1–10 min.

2 Data

A magnetometer chain that is located on the west coast of Greenland is operated by the Technical University of Denmark (DTU). These stations were first established in 1981–1986. Most of the magnetometers in this chain are variometers, except for three that are geomagnetic observatories (https://www.space.dtu.dk/English/Research/Scientific_data_and_models/Magnetic_Ground_Stations.aspx) that have accurate, absolute calibrations. Another chain is positioned on the East Antarctic plateau and is operated by Virginia Tech. The instrumentation is referred to as Autonomous Adaptive Low-Power Instrument Platforms (AAL-PIP) (Clauer et al., 2014), while the chain itself can be referred to as PENGUIn (Polar Experimental Network for Geospace Upper atmosphere Investigations). The six PENGUIn stations were flown to the remote Antarctic plateau in 2008–2016, at a pace of one to two per year, with some return visits for repairs. As illustrated in the photos by Clauer et al. (2014), the installation of these systems involved high altitude, cold-weather camping at each site. The AAL-PIP and Greenland data are both in sensor coordinates coordinates northward, eastward, and vertical (NEZ). The northward axis of the magnetometers are aligned with the local magnetic field and the Z axis is pointed downward, so that the orientation of the eastward axis (in local magnetic coordinates) results through the right-hand rule. The units of all components are nT.

By design the AAL-PIP stations were placed at the magnetic conjugate points of the existing Western Greenland stations, with are situated (approximately) along the 40° magnetic meridian. The intended coordinates for these stations was determined through use of the International Geomagnetic Reference Field (IGRF), while the final exact locations were determined by whatever landing sites the plane pilots deemed to be suitable. The three-letter site identification codes of the Greenland stations are derived from the location names in the local, native language and the codes for the Antarctic stations are simply numbered from 0 to 5 with a “PG” prefix. The geographic and magnetic coordinates of these stations are listed in Table 1. Magnetic apex coordinates are used (VanZandt et al., 1972; Richmond, 1995), derived from the IGRF 2015 model. The PENGUIn and Greenland magnetometer data have previously been used to investigate interhemispheric asymmetries in magnetic perturbations (Hartinger et al., 2016, 2017; Martines-Bedenko et al., 2018; Xu et al., 2017, 2020).

Table 1. Coordinates of the ground magnetometers used in this study

Northern Hemisphere Magnetometers					Southern Hemisphere Magnetometers				
Site ID	Geodetic		Geomagnetic[a]		Site ID	Geodetic		Geomagnetic[a]	
Code	°Lat.	°Lon.	°Lat.	°Lon.	Code	°Lat.	°Lon.	°Lat.	°Lon.
UPN	72.78	303.85	78.21	38.50	PG0	-83.67	88.68	-78.45	38.42
UMQ	70.68	307.87	75.62	41.07	PG1	-84.50	77.20	-77.06	37.51
GDH	69.25	306.47	74.46	38.08	PG2	-84.42	57.96	-75.34	39.22
ATU	67.93	306.43	73.18	37.03	PG3	-84.81	37.63	-73.61	36.82
SKT	65.42	307.10	70.58	36.26	PG4	-83.34	12.25	-70.88	36.46
GHB	64.17	308.27	69.12	36.95	PG5	-81.96	5.71	-69.49	37.31

[a]Geomagnetic locations are apex coordinates, calculated with the IGRF 2015 Model.

Interestingly, a comparison with the magnetic coordinates calculated with the IGRF 2020 model indicated that in five years the Antarctic sites had moved equatorward by $0.35-0.41°$, while the Greenland sites moved poleward by $0.12-0.16°$. Additionally, Global Positioning System (GPS) instrumentation included on the platforms also showed that the ice sheet on which the stations rest is slowly shifting. The speed varies from a few meters per year for the PG0, PG1, PG2, and PG3 (those closest to the poles) to a few tens of meters per year at PG4 and PG5, which are closest to the coast. Generally speaking, the stations move towards the coast, the closer to the coast the faster the speed. For PG3, PG4, and PG5 this is northeastward, toward Halley. PG2, PG1, and PG0 move more towards McMurdo.

3 Symmetric Magnetic Fields Observed at Magnetic Conjugate Points

Figure 1 shows an example of magnetic field measurements at both the PENGUIn sites and at the conjugate stations in the Northern hemisphere, taken on 16 November 2017. The blue lines in this graph show the magnetic fields measured in the Northern hemisphere at the sites indicated with the blue labels on the left side, and the red lines show the magnetic fields measured in the Southern hemisphere at the sites indicated with the red labels on the left side. Site locations are shown in Table 1. All three components are graphed. Baseline offsets have been subtracted if present. This figure demonstrates

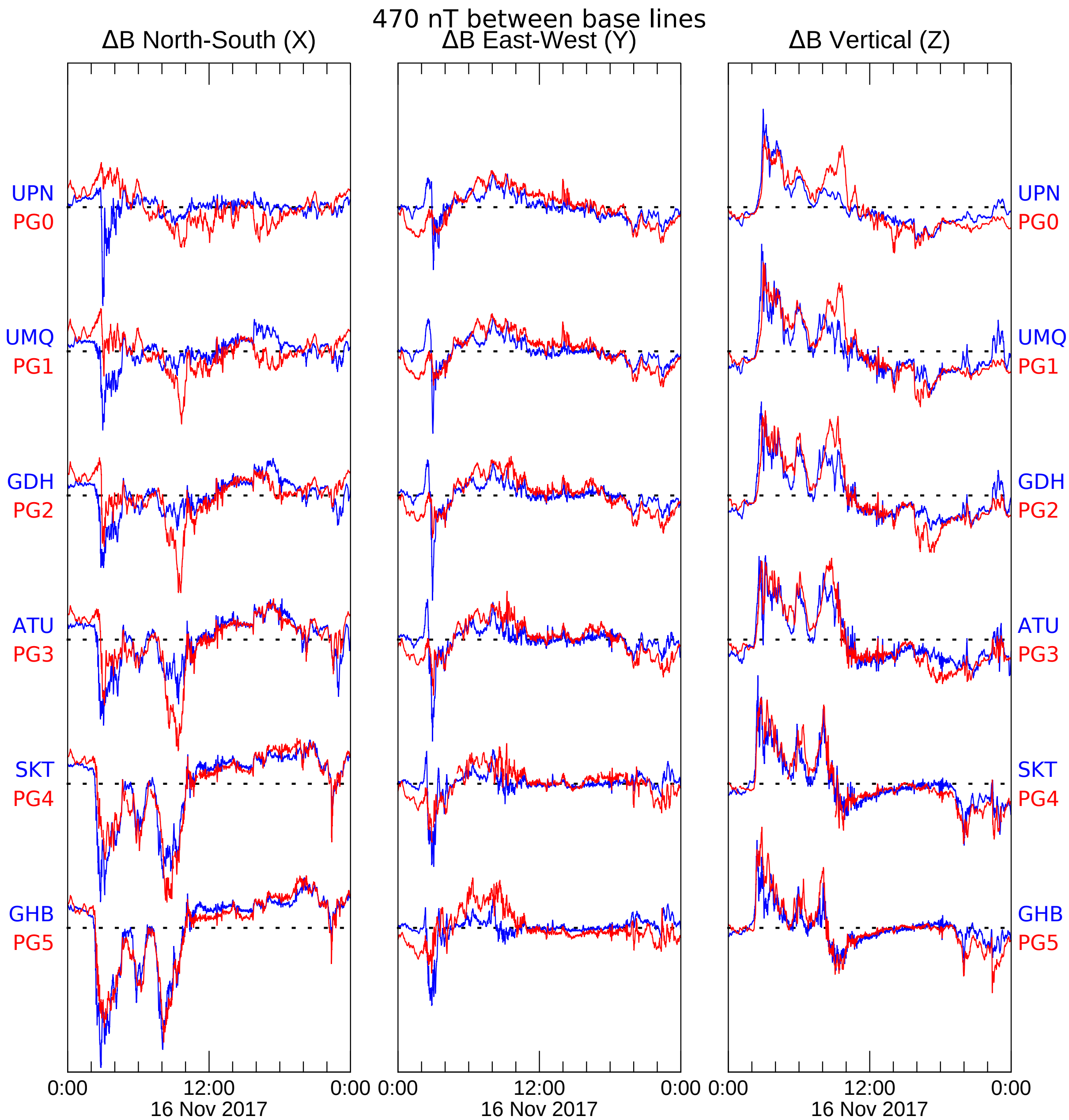

Figure 1. Symmetric magnetic fields observed at conjugate locations on 16 November 2017. The blue lines show the magnetic fields measured in the Northern hemisphere at the sites indicated with the blue labels on the left side, and the red lines show the magnetic fields measured in the Southern hemisphere at the sites indicated with the red labels on the left side. Site locations are shown in Table 1.

a case where the conjugate measurements are nearly the same, which indicates that the conjugate sites can indeed detect similar electrodynamic patterns in opposite hemispheres.

For example, the red and blue curves in Figure 1 exhibit very similar behavior at most station pairs. The magnetometers are detecting the effects of the Interplanetary Magnetic Field (IMF) merging with the Earth's magnetic field and the resulting flow of plasma and electromagnetic energy in the magnetosphere and ionosphere. Some differences between the hemispheres are to be expected due to seasonal differences in conductivity. The two most poleward sites at the top of Figure 1 have some disagreements; these sites are likely within an area of open magnetic field lines, while the more equatorward sites are on closed field lines. The Supplemental Information contains four additional graphs in which the conjugate sites have very similar variations.

One detail that hadn't been mentioned until now is the fact that the measurements in the southern hemisphere had their eastward and vertical components multiplied by -1 in order to obtain the agreements shown. The reasons for these sign changes are illustrated in Figure 2.

Starting with the northward component of ΔB in Figure 2(a), a Westward electrojet, or Hall current, is shown located near midnight in the polar graphs. In the Northern hemisphere the magnetic field underneath this electrojet is pointed away from the North pole, so this component has a negative sign. In the Southern hemisphere the magnetic field at ground level is actually located "above" the electrojet when viewed from above the North pole, as is the convention with polar graphs of the electrodynamic patterns that have 0 magnetic local time (MLT) at the bottom, 6 MLT at the right, and 12 MLT at the top. ΔB_n in this case points toward the Southern pole, but since the convention is that a positive ΔB_n points northward, then this component also has a negative sign.

The eastward component of ΔB is illustrated in Figure 2(b). This component typically has the smallest magnitude. While the electrojet near midnight MLT is typically in the Westward direction, it may have some tilt toward the pole or equator. In 2(b) the Hall current flows toward the equator, which produces a positive ΔB_e in the Northern hemisphere and a negative (westward) ΔB_e in the Southern hemisphere. Thus, ΔB_e in the south needs to have a sign flip in order to match the pattern in the north.

Finally, the vertical component of ΔB is illustrated in Figure 2(c). Previously D. R. Weimer et al. (2010) had found that the vertical component typically has a very good correlation with the overhead field aligned current (FAC) patterns (D. Weimer, 2001; D. R. Weimer,

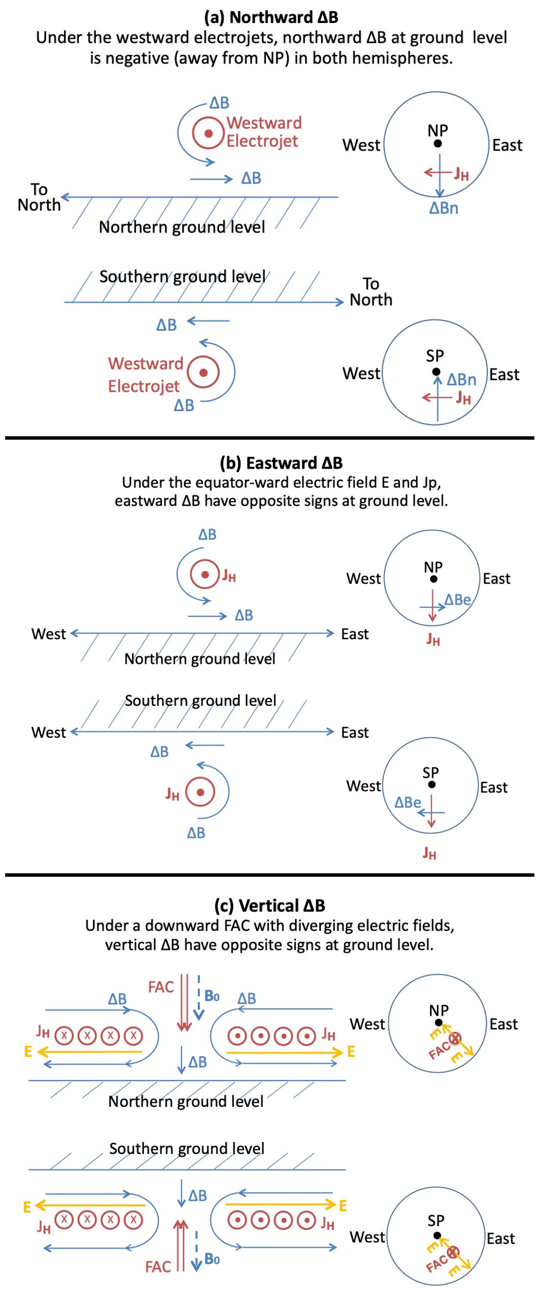

Figure 2. Explanation for eastward and vertical sign reversals. (a) Northward ΔB underneath a westward electrojet is negative in both hemispheres. (b) Eastward ΔB positioned underneath equatorward directed electrojet have opposite signs at the conjugate points. (c) Vertical ΔB underneath downward field alined currents (FAC) also have opposite signs.

2005a). In the Northern hemisphere, where the FAC flows into the ionosphere (positive) the vertical ΔB_Z is also positive (downward) and vice versa. Figure 2(c) shows a downward FAC on the dawn side in both the northern and southern hemispheres on the dawn side, which would be part of the Region 2 system (Iijima & Potemra, 1976). This downward FAC needs to close through diverging Pedersen currents that are shown in 2(c) as producing Pedersen currents and electric fields that point toward the equator on one side and toward the pole on the other side. The left side of 2(c) illustrates the Hall currents associated with these diverging electric fields, and the magnetic perturbations produced by these Hall currents. At the point directly under the FAC this perturbation points toward the ground in the north (positive ΔB_Z) and away from the ground (negative ΔB_Z). Thus, ΔB_Z in the south needs to have a sign change in order to match the pattern in the north. While the reasons for these sign changes are not intuitively obvious, the data shown in Figure 1 and the Supplemental Information confirm that they are necessary.

4 Broken Symmetry

In order for the symmetric magnetic field signatures to be present it is necessary for the magnitude of Z component of the IMF to be larger than the Y component. It is more common for the Y component to be dominant due to the sector structure of the solar wind and IMF. It is known that a strong Y component in the IMF produces a twisted magnetotail (White et al., 1998) and magnetopause (Siscoe et al., 2001), and electric potential patterns that differ between the two hemispheres (Siscoe et al., 2001; D. R. Weimer, 2005a). Thus, if a non-zero Y component is present with sufficient magnitude then the symmetry is broken between the magnetic fields observed at conjugate locations. Additionally, differences in the conductivity, due to unequal solar illumination in summer and winter, will also break the symmetry as well as the tilting of the dipole axis toward and away from the Sun.

Figure 3 shows an example of conjugate measurements from 3 December 2016 that do not agree, due to the influence of both the Y component of the IMF and the seasonal conductivity and tilt angle differences. The IMF measurements on the same day are shown in Figure 4. These data are from the Magnetic Field Instrument (MFI) (Smith et al., 1998) on the Advanced Composition Explorer (ACE) spacecraft. The IMF values are in the Geocentric Solar Magnetic (GSM) coordinate system. It is seen that the Z component (brown line at bottom) hovers around zero, while varying between -2 and +1 nT. The Y component (2nd from bottom, colored turquoise) varies between 1 and 4 nT. The solar wind velocity is plotted with the purple line in the third row from the bottom using data from the Solar Wind Electron, Proton, and Alpha Monitor (SWEPAM) on ACE

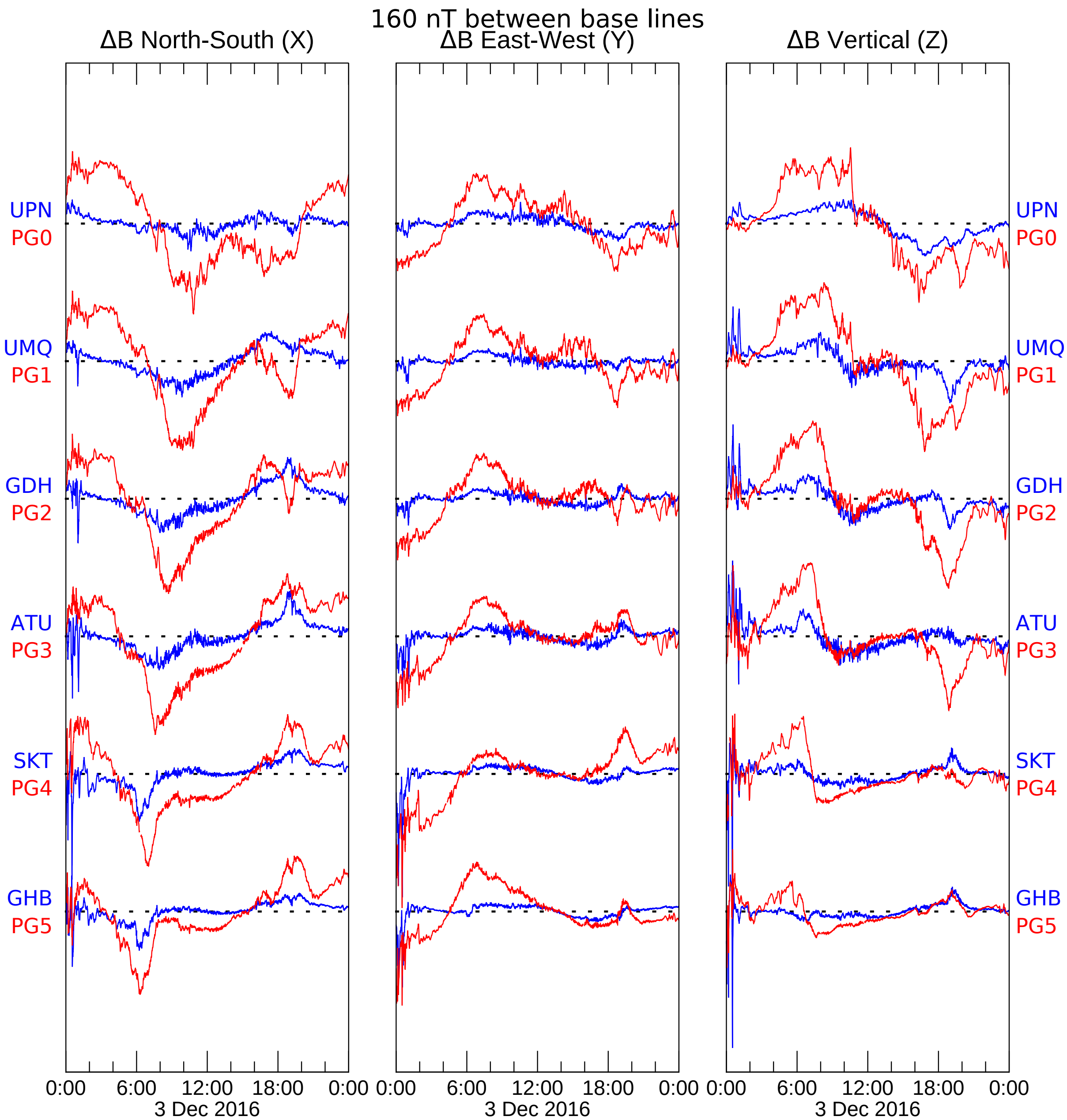

Figure 3. Unequal magnetic fields observed at conjugate locations on 3 December 2016. The blue lines show the magnetic fields measured in the Northern hemisphere at the sites indicated with the blue labels on the left side, and the red lines show the magnetic fields measured in the Southern hemisphere at the sites indicated with the red labels on the left side. Site locations are shown in Table 1.

(McComas et al., 1998). In Geocentric Solar Ecliptic (GSE) coordinates, the solar wind is moving in the -X direction (toward the Earth) at a fairly steady velocity of 300 km/sec.

The timeline on the abscissa axis indicates when the measurements were taken at the location of the ACE satellite, which is about $240R_E$ sunward from the Earth. The delay in time required for the solar wind, and the magnetic field that is embedded within, to reach the bow shock of the Earth is approximately 80 min, as shown with the green line at the top part of Figure 3.

The differences between the magnetic fields seen in the opposite hemispheres can be attributed to both the dominant Y component of the IMF as well as conductivity, with the southern hemisphere getting much more solar illumination in early December. To better understand the behavior of the measured magnetic fields we turn our focus to the time period of 7:00 to 19:00 UT on 3 December 2016. Figure 5 shows the Northward component of ΔB_X (northward) during this time at the four most poleward PENGUIn sites (PG0–PG3) that are shown with the red lines in the bottom four panels in Figure 3. The measurements at their conjugate counterparts in the Northern hemisphere are drawn in blue. The top two rows shows the Y and Z components of the IMF that have been time shifted by 78.1 min, the mean value of the time delay (top of Figure 4) during this interval. For future reference, marks at 8:00, 12:00, and 18:00 UT are indicated with the superposed thin lines.

Figure 6 shows maps of ground-level magnetic perturbation patterns and ionospheric electric potentials at the three times on 3 December 2016 which help to explain the observed variations. The maps in the top and third row show the northward component of ΔB in the Northern and Southern hemispheres respectively that are derived using the empirical model by D. R. Weimer (2013). The maps in the second and forth (bottom) rows show the electric potential pattens from the empirical model by D. R. Weimer (2005b). The maps are generated using the mean of the IMF and solar wind values over the previous 20 minutes, after adding another 20 minutes to the propagation delay, that accounts for transmission of the electrodynamic signal through the bow shock and then from the magnetopause to the polar ionospheres (D. R. Weimer et al., 2010). The Southern hemisphere maps use IMF B_Y values in the model inputs that have their signs flipped from the values used in north, and the dipole tilt angle is also reversed.

These maps are intended to show the context of the magnetic field measurements with respect to the mapped patterns, rather than for any comparison of exact values. It is seen in Figure 6(a) that at 08:00 UT the northern chain is situated in a region of

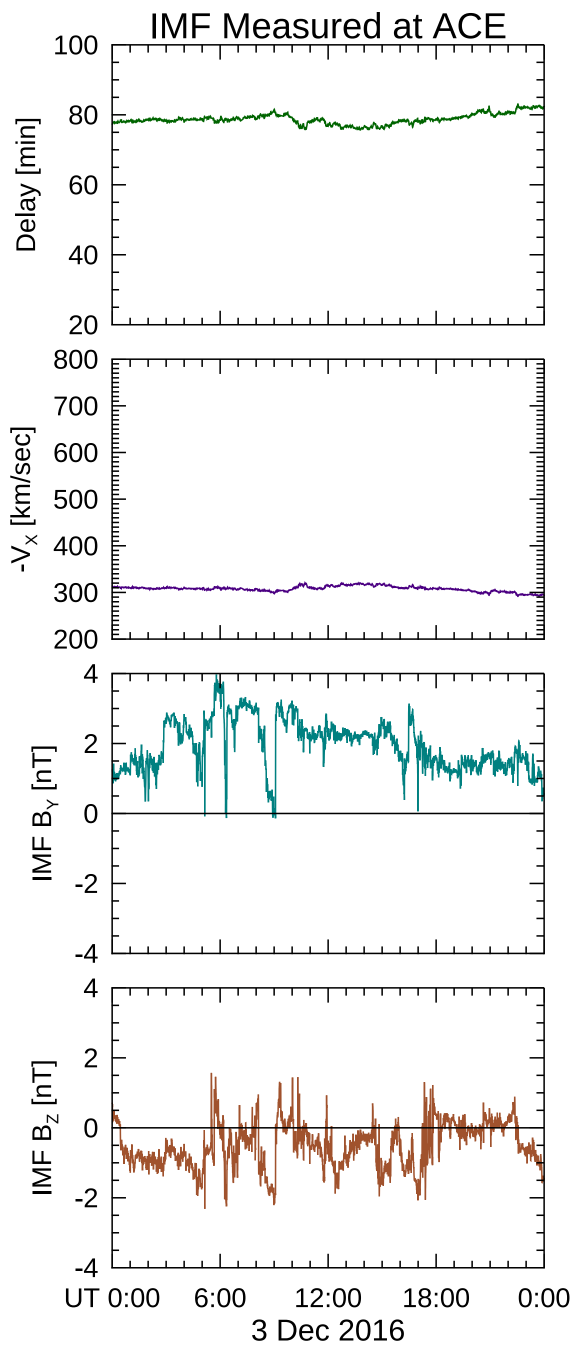

Figure 4. IMF measurements taken on the ACE satellite, 3 December 2016. From bottom to top: The Z component of the IMF, drawn in brown (sienna). The Y component of the IMF, colored turquoise. The -X component of the solar wind velocity (purple). At the top, the green line shows the propagation delay, in minutes, from the point of measurement to the Earth.

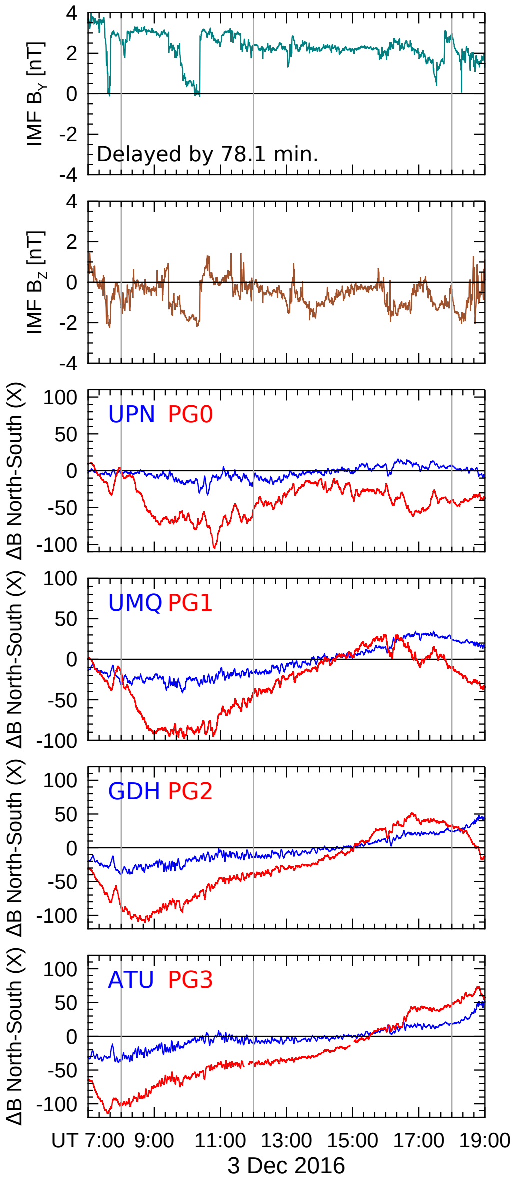

Figure 5. Y and Z components of the IMF and the X (Northward) component of ΔB at four conjugate locations, from 7:00 to 19:00 UT on 3 December 2016. The upper two rows show the Y and Z components of the IMF, colored turquoise and brown respectively, and shifted in time by 78.1 min. The other four graphs show the Northward component of ΔB at the four most poleward PENGUIn sites (drawn in red) and their Northern counterparts (blue). The thin vertical lines mark three times that are referenced in Figure 6.

negative ΔB_N. At 18:00 UT in 6(c) they have moved to a region of mostly positive ΔB_N, with the northernmost end of the chain near the transition between positive and negative, in qualitative agreement with the measurements shown in Figure 5. The south-

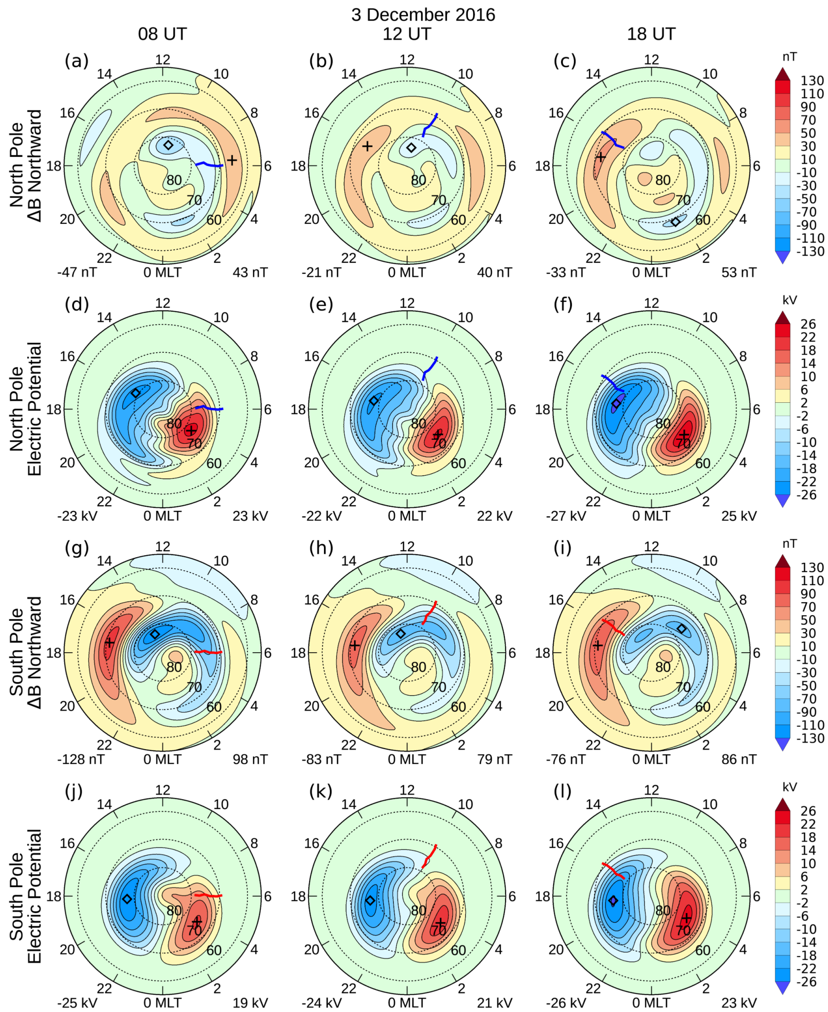

Figure 6. Maps of the (Northward) component of ΔB and electric potentials in both hemispheres. These maps are for 08:00 UT (left column), 12:00 UT (center column), and 18:00 UT (right column) on 3 December 2016. The maps in the top row show the Northward component of ΔB at the thee times listed, with the location of the Greenland chain in magnetic latitude-local time coordinates superposed on the map with a blue line. The second row shows the electric potentials in the Northern hemisphere, with the magnetometer locations superposed. The third row shows the Northward component of ΔB, with the location of the Antarctic chain marked with a red line. The bottom row shows the electric potentials in the Southern hemisphere. Minimum and maximum values of the mapped quantities are indicated in the lower left and right corners of each polar map.

ern chain at 08:00 UT in 6(g) mostly lies in a more strongly negative ΔB_N, with the most poleward end positioned near a transition to a positive region. At 18:00 UT in 6(i) the southern sites have moved to a region of positive ΔB_N at the low latitude end while the poleward sites cross zero into negative territory, in agreement with Figure 5. Throughout this day the higher conductivity in the souther hemisphere obviously influences the larger magnetic field values that are seen. The influence of IMF B_Y is most apparent at 18 UT, and the changes seen throughout the day are mostly the result of the sites simply moving in local time.

5 IMF B_Y Step Transitions

Another case in which the Y component of the IMF has an even greater influence on the observed asymmetry is shown in Figure 7, in the same format as Figures 1 and 3, from 4 February 2016. The IMF measurements on the same day, 4 February 2016, are shown in Figure 8, in the same format as Figure 4. The Z component fluctuates around a value of +5 nT during most of the day, except for a period from approximately 09:00 to 15:00 UT when it drops to less than zero on two occasions. The Y component is in the range of +5 to +8 nT through most of the day, except for a prominent transition to -5 nT for just over two hours before flipping back to +5 nT. The solar wind velocity, shown with the purple line in the third row from the bottom, runs between 400 to 480 km/sec. This velocity results in a time delay for the solar wind to reach the bow shock of the Earth in approximately 50 min, as shown with the green line in the top row, if it is assumed that the IMF fluctuations lie within a flat plane that is perpendicular to the flow direction.

As found by D. R. Weimer et al. (2002), the IMF transitions often lie within planes that are tilted at varying angles with respect to the Earth-Sun line (GSE X axis) rather than perpendicular, which results in complicated variations in the propagation times. The magenta-colored line that is superposed in the top row shows the expected time delays that take these tilted orientations into consideration, using the method outlined by D. R. Weimer and King (2008). Refer to the articles and illustrations therein by J. Borovsky (2008) and J. E. Borovsky (2018) for a description of the geometrical structure of the of the IMF that causes the variations in the propagation times. This modification to the delays is included in Figure 8 due to the need for more accurate timings later in this paper.

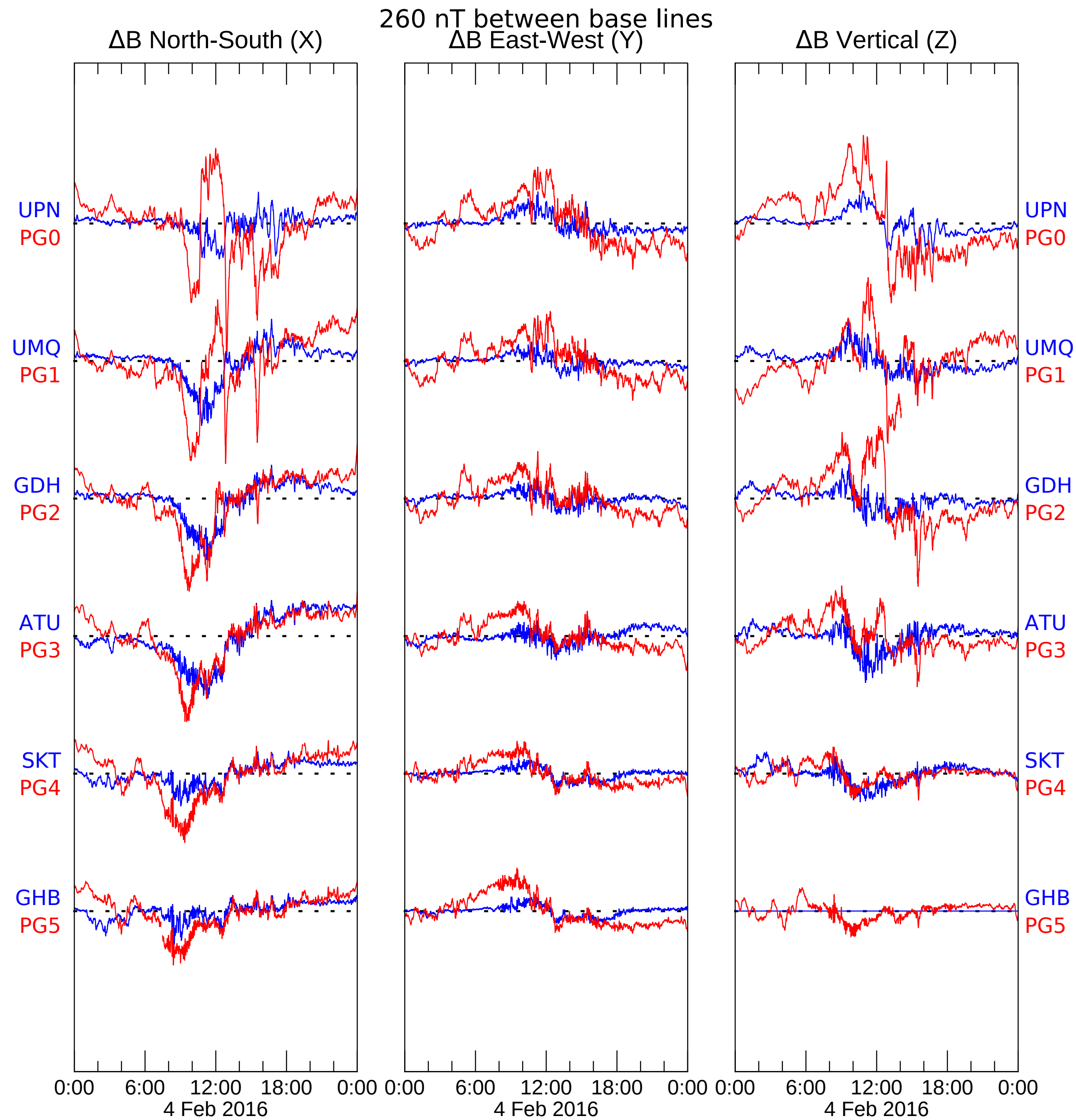

Figure 7. Unequal magnetic fields observed at conjugate locations on 4 February 2016. The blue lines show the magnetic fields measured in the Northern hemisphere at the sites indicated with the blue labels on the left side, and the red lines show the magnetic fields measured in the Southern hemisphere at the sites indicated with the red labels on the left side. Site locations are shown in Table 1.

Figure 9 shows a closer look at the time period around the IMF B_Y transitions on 4 February 2016, from 09:00 UT to 14:00 UT. The format of this figure is similar to that

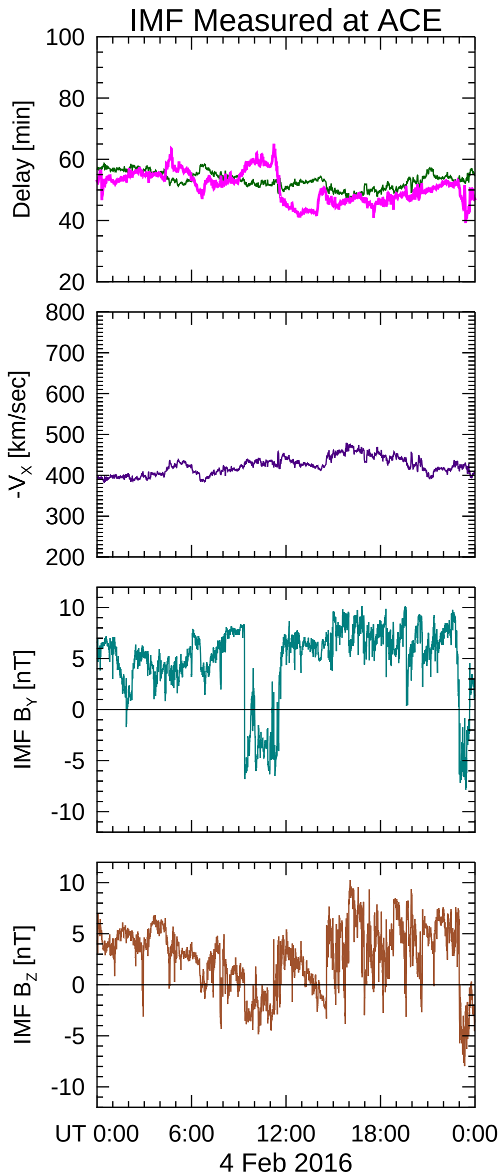

Figure 8. IMF measurements taken on the ACE satellite, 4 February 2016. From bottom to top: The Z component of the IMF, drawn in brown. The Y component of the IMF, colored turquoise. The X component of the solar wind velocity (purple). At the top, the green line shows the "flat plane" propagation delay, in minutes from the point of measurement at L1 to the Earth, and the superposed magenta line show the propagation delay that accounts for phase front tilt angles.

in Figure 5, with the four bottom rows showing the northward component of ΔB at the four most poleward PENGUIn sites (PG0–PG3) drawn with the red lines while the North-

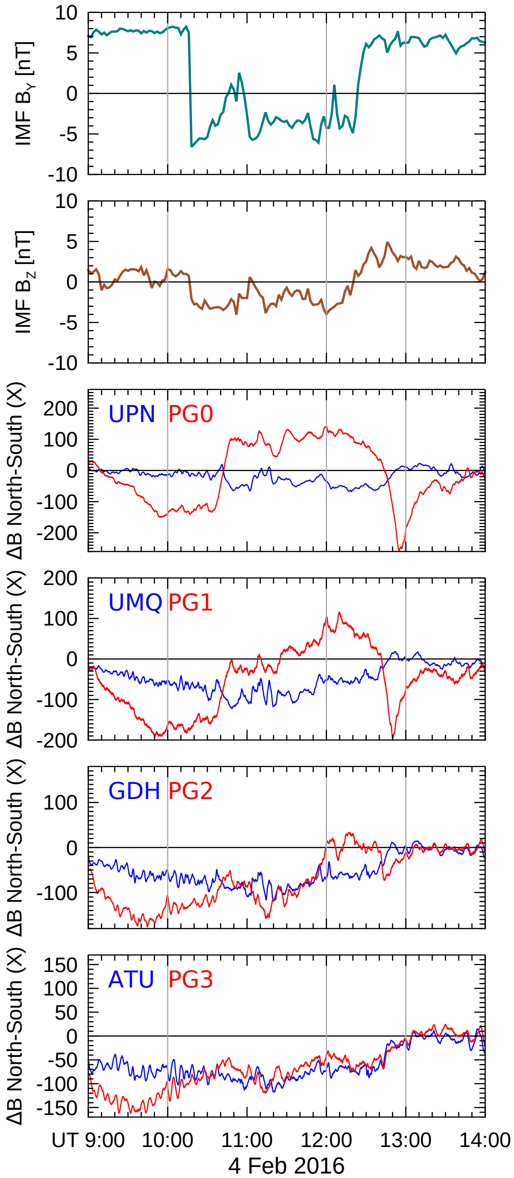

Figure 9. Y component of the IMF and the X (Northward) component of ΔB at four conjugate locations, from 09:00 to 14:00 UT on 4 February 2016. The upper two rows show the Y and Z component of the IMF drawn in turquoise and brown, shifted in time to the bow shock using variable lags. The other four graphs show the Northward component of ΔB at the four most poleward PENGUIn sites (drawn in red) and their Northern counterparts (blue). Dotted lines on the time axis mark three times at 10:00, 12:00, and 13:00 UT that are referenced in Figure 10.

ern hemisphere data are drawn in blue. The top two rows shows the Y and Z components of the IMF drawn with turquoise and brown colors. These IMF data have been shifted in time to the position of the solar wind bow shock in front of the Earth, using

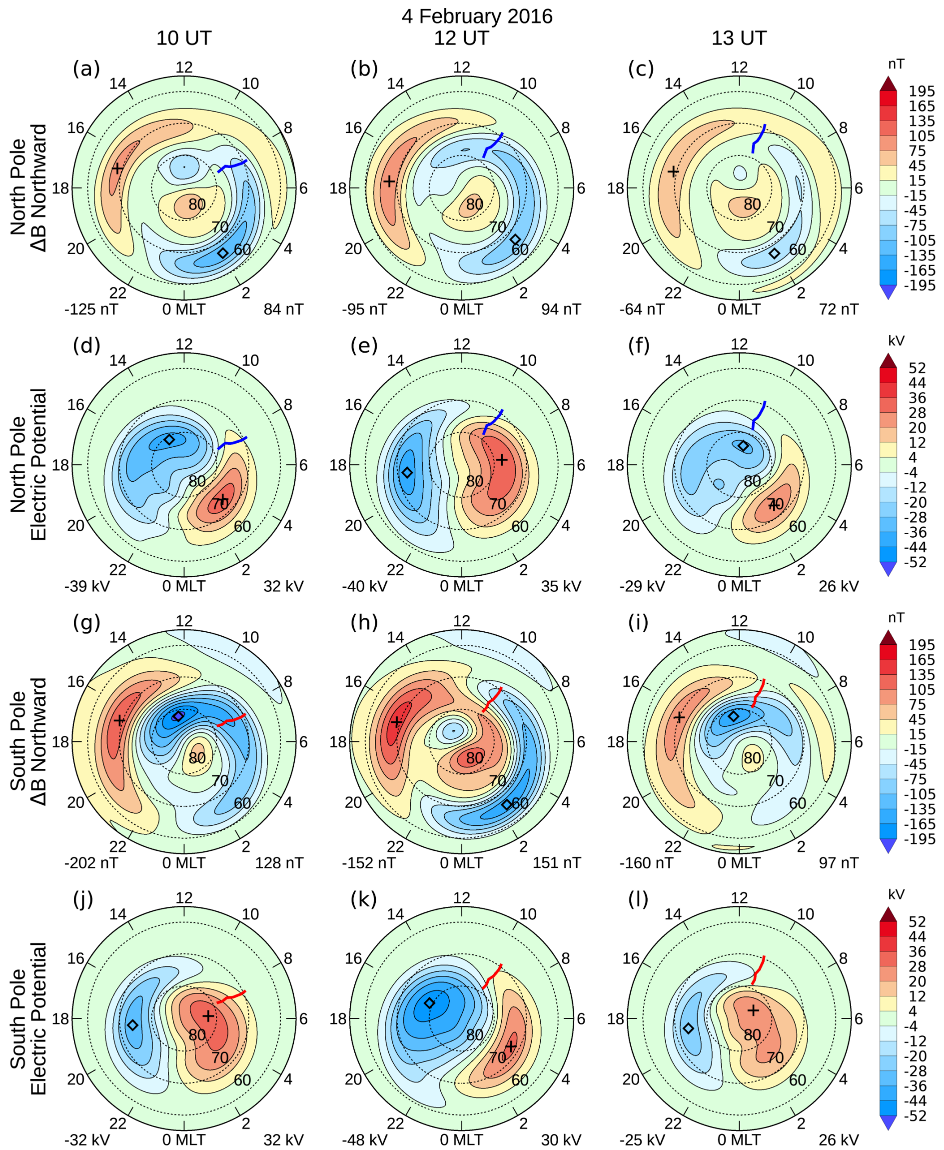

Figure 10. Maps of the (Northward) component of ΔB and electric potentials in both hemispheres. These maps are for 10:00 UT (left column), 12:00 UT (center column), and 13:00 UT (right column) on 4 February 2016. The format of this figure is the same as Figure 6.

the variable timings shown in Figure 8. Reference marks at 10:00, 12:00, and 13:00 UT are indicated on the horizontal axis using dotted lines. The first mark at 10:00 UT is just before IMF Y flips from positive to negative, 12:00 UT is near the end of the negative time interval (during which the electrodynamic pattern has had time to reconfigure), and 13:00 UT is approximately a half-hour after the transition of IMF Y back to a positive value.

Figure 10 shows maps of ground-level magnetic perturbation patterns and ionospheric electric potentials on 4 February 2016 at the three times just mentioned. The format of this figure is the same as in Figure 6. As before, the maps in this figure show an overview of the northern and southern magnetometer chain locations with respect to the global electric potential and magnetic perturbation patterns. At 10:00 UT the northern chain is situated in a region of negative ΔB_N, except at the most poleward site which is near zero, as seen in 10(a). The measurements shown with the blue lines in Figure 9 at this time are in agreement, with the UPN site being located the most poleward. The southern chain in 10(g) is positioned entirely within a region of negative ΔB_N but having a larger magnitude. This southern chain is positioned within the dawn electric potential cell in 10(j), while the northern chain in 10(d) is at the dayside end of the dawn cell and extending into the anti-sunward plasma flow.

In 10(b) at 12:00 UT, after IMF B_Y flips from positive to negative, the northern chain is now in a region of more strongly negative ΔB_N. Figure 10(h) shows that the southern chain at this time is in the negative region at the more equatorward end, while the more poleward end is in the positive part of the map, in agreement with data shown in Figure 9.

After the IMF B_Y flips back to positive, by 13:00 UT the northern chain extends from weakly positive at the low latitude end to near zero at the poleward end, as illustrated with the blue lines in Figures 9 and 10(c). At the same time, 10(i) shows that the southern chain transitions from near zero at the equatorward end to strongly negative at the poleward end, also in agreement with Figure 9.

6 Time Lags and Response Times

The sharp transitions in IMF B_Y on 4 February 2016 provide an opportunity to reexamine the time lags between changes in the IMF and the observed ground-level magnetic response. From enlarged versions of Figure 9 (not shown) it was found that B_Y flips from positive to negative at 10:17 UT while the magnetic field at the PG0 and PG1 sites start to increase from negative toward positive 18 min later, at 10:35 UT. These transitions reach their peak 13 min later at 10:48 UT. The lags at the northern sites UPN and UMQ are similar, but difficult to ascertain with certainty due to the much smaller variations in the winter hemisphere. At the more equatorward sites in both hemispheres the changes in the magnetic fields are unremarkable.

At the next IMF transition B_Y crosses zero going positive at 12:23 UT, while at the same time B_Z is also moving from negative to positive. At southern sites PG0 and PG1 the measured ΔB_N have been decreasing since 12:00 UT, and then at 12:41 UT the rate of change accelerates. Again, this change occurs 18 min after the IMF B_Y flip. The most negative value is reached 14 min later at 12:55 UT at PG0, and after 9 min at 12:50 UT at PG1, with similar but much smaller responses seen at the northern conjunction sites. Speculating, PG1 may have reacted faster than PG0 by being located closer to the center of the anti-sunward convection "throat" in Figure 10(k).

7 Discussion and Conclusion

It has long been assumed that the ionospheres in the northern and southern hemispheres have similar electrodynamic patterns. Under some conditions the magnetic perturbations at opposite ends of the magnetic field lines are expected to be similar. The placement of the PENGUIn magnetometers at locations conjugate to stations on the west coast of Greenland provided an opportunity to verify these assumptions. The results presented here (and in Supplemental Information figures) confirm that the conjugate sites do have identical or similar (symmetric) magnetic perturbations under the right conditions. We've shown that sign reversals are required for the Y (eastward) and Z (downward) components in order to obtain this agreement. More often than not, a dominant IMF B_Y can break the symmetry, as well as the presence of unequal conductivities in the opposite hemispheres. Statistical maps of electric potentials and magnetic perturbations are shown to be useful for explaining the temporal changes that occur in both hemispheres. During the course of the day, it is often the movement of magnetometers in local time that causes the observed variations. It would be possible to use numerical simulations and other models in a similar manner to provide the context of the magnetometer locations with respect to the global patterns.

In one event the Y component of the IMF flipped from strongly positive to strongly negative, and back again about two hours later, while the northern and southern magnetometer chains were approaching noon in local time. This fortuitous occurrence provided a unique opportunity to observe the broken symmetry at the conjugate locations and to measure the time lags between the IMF transitions and the resulting magnetic field reaction. It was found that the magnetic fields at most poleward sites started to respond to the sudden IMF changes after 18 min, a measure of the time it takes for the electromagnetic signal in the solar wind and embedded IMF to reach the magnetopause, after travel from the bow shock through the magnetosheath, and then propagate along magnetic field lines to the polar ionospheres. The propagation delay is also referred to as the "communication time," which can be in the range of 8–14 min (Ridley et al., 1998). An additional 9 to 14 min is required for the magnetic perturbations to complete the transition. The time delays are longer at the more equatorward locations. These results agree with previous findings by Ridley et al. (1998), D. R. Weimer et al. (2010), and references therein, but with better temporal resolution.

Space science investigations have long relied on magnetometer measurements in the northern hemisphere to indirectly observe the flow of currents in the ionosphere and magnetosphere. It has only been more recently that it has been possible to acquire magnetic field measurements in the southern polar region in order to observe hemispheric similarities and differences. While there are substantial engineering and logistical challenges in putting magnetometers on the Antarctic plateau (Clauer et al., 2014), the expansion and maintenance of such infrastructure will advance future research which will yield insight into the causes and consequences of multi-scale hemispheric asymmetries"

Open Research Section

The magnetometer data are available at these web sites:

`http://mist.nianet.org`

`http://128.173.89.68:48000/`

`https://www.space.dtu.dk/English/Research/`

`https://ftp.space.dtu.dk/data/`

The interplanetary magnetic field and solar wind measurements from the ACE spacecraft can be obtained at `https://cdaweb.gsfc.nasa.gov/pub/data/ace/`

The Weimer 2005 electric potential model is available at `https://doi.org/10.5281/zenodo.2530324`, and maps produced by the Weimer 2013 magnetic perturbation model are available at `https://doi.org/10.5281/zenodo.3985988`.

Acknowledgments

This work was funded by NSF grants OPP-1543364, OPP-1744828, and AGS-2027168 to Virginia Tech. MDH was supported by NSF grant AGS-2027210.

References

Borovsky, J. (2008). The flux-tube texture of the solar wind: strands of the magnetic carpet at 1 AU? *J. Geophys. Res.*, *113*. doi: 10.1029/2007JA012684

Borovsky, J. E. (2018). The spatial structure of the oncoming solar wind at Earth and the shortcomings of a solar-wind monitor at L1. *Journal of Atmospheric and Solar-Terrestrial Physics*, *177*, 2 – 11. doi: 10.1016/j.jastp.2017.03.014

Clauer, C. R., Kim, H., Deshpande, K., Xu, Z., Weimer, D., Musko, S., ... Ridley, A. J. (2014). An autonomous adaptive low-power instrument platform (AAL-PIP) for remote high-latitude geospace data collection. *Geoscientific Instrumentation, Methods and Data Systems*, *3*(2), 211–227. Retrieved from `https://gi.copernicus.org/articles/3/211/2014/` doi: 10.5194/gi-3-211-2014

Hartinger, M. D., Clauer, C. R., & Xu, Z. (2016, October). Space weather from a southern point of view. *Eos*, *97*. doi: 10.1029/2016EO061791

Hartinger, M. D., Xu, Z., Clauer, C. R., Yu, Y., Weimer, D. R., Kim, H., ... Willer, A. N. (2017). Associating ground magnetometer observations with current or voltage generators. *Journal of Geophysical Research: Space Physics*, *122*(7), 7130–7141. Retrieved from `https://agupubs.onlinelibrary.wiley.com/doi/abs/10.1002/2017JA024140` doi: https://doi.org/10.1002/2017JA024140

Iijima, T., & Potemra, T. A. (1976). The amplitude distribution of field aligned currents at northern high latitudes observed by Triad. *J. Geophys. Res.*, *81*, 2165–2174. doi: 10.1029/JA081i013p02165

Laundal, K., Cnossen, I., Milan, S., Haaland, S., Coxon, J., Pedatella, N., ... Reistad, J. (2017). North–South asymmetries in Earth's magnetic field. *Space Science Reviews*, *206*, 225–257. Retrieved from `https://doi.org/10.1007/s11214-016-0273-0` doi: 10.1007/s11214-016-0273-0

Martines-Bedenko, V. A., Pilipenko, V. A., Hartinger, M. D., Engebretson, M. J., Lorentzen, D. A., & Willer, A. N. (2018). Correspondence between the latitudinal ulf wave power distribution and auroral oval in conjugate ionospheres. *Sun and Geosphere*, *13*(1), 41–47. Retrieved from `https://par.nsf.gov/biblio/10057802`

McComas, D. J., Bame, S. J., Barber, P., Feldman, W. C., Phillips, J. L., & Riley,

P. (1998). Solar wind electron, proton, and alpha monitor (SWEPAM) on the Advanced Composition Explorer. In C. T. Russell, R. A. Mewaldt, & T. T. V. Rosenvinge (Eds.), *The Advanced Composition Explorer Mission.* Dordrecht: Springer. doi: https://doi.org/10.1007/978-94-011-4762-0_20

Ostgaard, N., & Laundal, K. M. (2012). Auroral asymmetries in the conjugate hemispheres and interhemispheric currents. In *Auroral phenomenology and magnetospheric processes: Earth and other planets* (pp. 99–112). American Geophysical Union (AGU). Retrieved from `https://agupubs.onlinelibrary.wiley.com/doi/abs/10.1029/2011GM001190` doi: 10.1029/2011GM001190

Richmond, A. D. (1995). Ionospheric electrodynamics using magnetic apex coordinates. *J. Geomag. Geoelectr.*, *47*, 191. doi: 10.5636/jgg.47.191

Ridley, A. J., Lu, G., Clauer, C. R., & Papitashvili, V. O. (1998). A statistical study of the ionospheric convection response to changing interplanetary magnetic field conditions using the assimilative mapping of ionospheric electrodynamics technique. *J. Geophys. Res.*, *103*(A3), 4023–4039. Retrieved from `https://doi.org/10.1029/97JA03328` doi: 10.1029/97JA03328

Siscoe, G. L., Erickson, G. M., Sonnerup, B. U. O., Maynard, N. C., Siebert, K. D., Weimer, D. R., & White, W. W. (2001). Global role of $E_{\|}$ in magnetopause reconnection: An explicit demonstration. *J. Geophys. Res.*, *106*(A7), 13015–13022. Retrieved from `https://doi.org/10.1029/2000JA000062` doi: 10.1029/2000JA000062

Smith, C. W., L'Heureux, J., Ness, N. F., Acuna, M. H., Burlaga, L. F., & Scheifele, J. (1998). The ACE Magnetic Field Experiment. In C. T. Russell, R. A. Mewaldt, & T. T. V. Rosenvinge (Eds.), *The Advanced Composition Explorer Mission.* Dordrecht: Springer. doi: https://doi.org/10.1007/978-94-011-4762-0_21

VanZandt, T. E., Clark, W. L., & Warnock, J. M. (1972). Magnetic apex coordinates: A magnetic coordinate system for the ionospheric f_2 layer. *Journal Of Geophysical Research-Space Physics*, *77*, 2406. doi: 10.1029/JA077i013p02406

Weimer, D. (2001). Maps of field-aligned currents as a function of the interplanetary magnetic field derived from Dynamic Explorer 2 data. *J. Geophys. Res.*, *106*, 12,889. doi: 10.1029/2000JA000295

Weimer, D. R. (2005a). Improved ionospheric electrodynamic models and application to calculating Joule heating rates. *J. Geophys. Res.*, *110*. doi: 10.1029/2004JA010884

Weimer, D. R. (2005b). Predicting surface geomagnetic variations using ionospheric electrodynamic models. *J. Geophys. Res.*, *110*. doi: 10.1029/2005JA011270

Weimer, D. R. (2013). An empirical model of ground-level geomagnetic perturbations. *Space Weather*, *11*, 107–120. Retrieved from https://doi.org/10.1002/swe.20030 doi: 10.1002/swe.20030

Weimer, D. R., Clauer, C. R., Engebretson, M. J., Hansen, T. L., Gleisner, H., Mann, I., & Yumoto, K. (2010). Statistical maps of geomagnetic perturbations as a function of the interplanetary magnetic field. *J. Geophys. Res.*, *115*. doi: 10.1029/2010JA015540

Weimer, D. R., & King, J. H. (2008). Improved calculations of interplanetary magnetic field phase front angles and propagation time delays. *J. Geophys. Res.*, *113*. doi: 10.1029/2007JA012452

Weimer, D. R., Ober, D. M., Maynard, N. C., Burke, W. J., Collier, M. R., McComas, D. J., … Smith, C. W. (2002). Variable time delays in the propagation of the interplanetary magnetic field. *J. Geophys. Res.*, *107*((A8)). doi: 10.1029/2001JA009102

White, W. W., Siscoe, G. L., Erickson, G. M., Kaymaz, Z., Maynard, N. C., Siebert, K. D., … Weimer, D. R. (1998). The magnetospheric sash and the cross-tail S. *Geophys. Res. Lett.*, *25*, 1605–1608. Retrieved from https://doi.org/10.1029/98GL50865 doi: 10.1029/98GL50865

Xu, Z., Hartinger, M. D., Clauer, C. R., Peek, T., & Behlke, R. (2017). A comparison of the ground magnetic responses during the 2013 and 2015 St. Patrick's Day geomagnetic storms. *Journal of Geophysical Research: Space Physics*, *122*(4), 4023–4036. Retrieved from https://agupubs.onlinelibrary.wiley.com/doi/abs/10.1002/2016JA023338 doi: https://doi.org/10.1002/2016JA023338

Xu, Z., Hartinger, M. D., Oliveira, D. M., Coyle, S., Clauer, C. R., Weimer, D., & Edwards, T. R. (2020). Interhemispheric asymmetries in the ground magnetic response to interplanetary shocks: The role of shock impact angle. *Space Weather*, *18*(3), e2019SW002427. Retrieved from https://agupubs.onlinelibrary.wiley.com/doi/abs/10.1029/2019SW002427 doi:

https://doi.org/10.1029/2019SW002427